Dynamic modeling of the first cell of a solar-assisted multi-effect distillation (MED) plant

Alberto de la Calle[a,*], Javier Bonilla[a], Lidia Roca[a], Patricia Palenzuela[b]

[a] *CIEMAT - Plataforma Solar de Almería, Ctra. de Senés s/n 04200 Tabernas, Almería, Spain*
[b] *Laboratorio de Investigaciones Medioambientales de Zonas Áridas, Escuela Universitaria de Ingeniería Industrial, Informática y Sistemas, Universidad de Tarapacá, Avda. General Velázquez 1775, Arica, Chile*

Abstract

This paper describes a model to simulate the thermal transient behavior of the first cell of a solar-assisted MED plant. It has been designed according to the experience with an experimental solar thermal desalination system erected at CIEMAT-Plataforma Solar de Almería (PSA). The non-linear first principles model has been developed using the object-oriented Modelica language. It includes two submodels corresponding to the effect and the preheater of the first cell of the MED plant. Both submodels have been calibrated and validated with experimental data. The numerical predictions show a good agreement with measured data.

Keywords: solar desalination, falling film evaporation and condensation, object-oriented modeling

1. Introduction

The alleviation of the lack of potable water in areas with high water-stress is a challenge nowadays. Seawater desalination is one of the possible solutions for regions close to sea, but, the high energy consumption and environmental pollution of this process are some of the disadvantages that researchers try to face. Coupling desalination plants with renewable energies is a way to avoid these disadvantages. It is usual to find high insolation levels in high water-stress areas, which makes solar thermal energy one of the most promising alternatives [1].

Solar thermal desalination consists of a solar thermal system coupled with a conventional thermal desalination process [2]. Although this technology can be found in an integrated system (direct solar desalination), the majority of the large scale applications have two separated devices, the solar collector and the distiller (indirect solar desalination) [3]. Among thermal desalination technologies, MED technology is preferred in most of the large scale solar thermal plants due to its low top-brine-temperature (TBT), typically less than 80°C, and its low specific energy consumption requirements [3].

Different types of solar collectors can be coupled with MED plants. In most of them, the device captures the solar radiation and transfers this heat to a fluid. The fluid can be either water or synthetic oil which is usually stored in an insulated thermal tank or other kind of thermal storage system [4]. The solar collector or the storage system can be connected to the MED unit directly or to a heat exchanger indirectly.

*Corresponding author. Tel.:+34 950 387 900; Fax: +34 950 365 300

Email addresses: alberto.calle@psa.es (Alberto de la Calle), javier.bonilla@psa.es (Javier Bonilla), lidia.roca@psa.es (Lidia Roca), patricia.palenzuela@psa.es (Patricia Palenzuela)

Although there are many variations of MED plants, the distillate process is similar in all of them. The plant is composed of a number of elements called effects which are connected between them. The steam produced in one effect is used as the heat source of the next effect, so, while in one hand, the incoming steam is condensing, on the other, the seawater is boiling producing more steam. This is possible because each effect has lower pressure than the previous one [1].

To improve the efficiency of the process, mathematical models and computer simulations can provide detailed information of the performance of the plant over a wide range of operating conditions. Several steady-state models have been published covering a wide variety of them. El-Dessouky and Ettouney [5, 6] published several contributions in steady-state modeling and simulation of MED processes. Recently, some authors have applied their respective models to improve the process [7, 8, 9, 10]. El-Nashar [11, 12] and Palenzuela et al. [13, 14] validated their respective models with experimental data.

Regarding dynamic modeling, the literature is scarce. El-Nashar and Qamhiyeh [15] developed a model for the study of the transient behavior of a multi-effect stack-type distillation plant. The results were compared with real data obtaining a reasonable agreement. Aly and Marwan [16] developed a dynamic model for a multi-effect process which has been the basis for other dynamic models, such as the six-effect evaporator model of paper industry developed by Kumar et al. [17]. Kishore et al. [18] presented the work-in-progress of a simulator for the steady state and the dynamics of a multi-effect distillation mechanical vapour compression (MED-VC) desalination system, showing a dynamic simulation of a single effect. Roca et al. [19] developed a dynamic model of a multi-effect distillation plant based on the heat transfer correlations obtained in [13]. This model is an improved version of a previous one in which the heat transfer coefficients were treated as constants [20]. It was developed with the object-oriented Modelica language and its main purpose was the prediction of the thermal dynamics of the heater and the distillate production rate. Kim et al. [21] presented a simulation model for predicting transient behavior of a solar-assisted MED plant. The model, which was focused on the long-term thermal and performance analyses, includes an evacuated-tube collector, a plate heat exchanger, storage tanks and a MED plant.

In this study, we focus on the first effect of a solar-assisted MED plant. This effect, also called heater, is the key to predict the thermal consumption of the MED unit due to its condition as heat exchanger between the solar field/storage system and the MED plant. In order to study its performance in different scenarios and design operating strategies to improve its efficiency, a new dynamic model of a first cell has been developed. This non-linear first principles model has been implemented with the object-oriented Modelica language. It uses as inputs the hot water flow, the feed seawater flow and the outlet pressure. The model is based on the AQUASOL experimental solar desalination system [22] and it has been calibrated and validated with experimental data. It predicts the thermal behavior of the first cell and its low computational effort allows fast simulation for control purposes.

2. Description of the plant

With the aim of testing and developing the solar thermal MED process, an experimental solar thermal desalination system was built at CIEMAT-Plataforma Solar de Almería at the early nineties [23]. Some modifications of the original plant were carried out within the AQUASOL project whose main objective was the development of a hybrid solar-gas desalination system that meets at the same time the requirements of low-cost, high efficiency and zero discharge [22].

The current configuration of the experimental solar thermal desalination plant permits a 24-h MED plant operation (cf. Fig. 1). The system is flexible regarding the energy supply of the plant and three

operating mode are possible:

- Solar-only mode: A compound parabolic collector (CPC) solar field provides all the thermal energy required.
- Fossil-only mode: A propane gas boiler by means of a double effect absorption heat pump (DEAHP) supplies the heat required by the MED plant. The DEAHP is coupled with the last effect of the MED plant recovering part of the energy. In this mode, the DEAHP can be connected to the MED plant directly or through the tanks indirectly.
- Hybrid mode: The energy comes from both the DEAHP and the solar field. The DEAHP permits a part-load operation from 30% to 100% strangling the steam flow between the boiler and the DEAHP.

Recently, a new operating mode has been tested at PSA [24]. With the aim of reducing the gas consumption, the gas boiler was replaced by a steam generator which was supplied by a small parabolic trough collector (PTC) solar field.

The desalination plant consists of a forward-feed MED unit with preheaters (Fig. 2). The plant has 14 effects in a vertical arrangement (Fig. 3) in which the seawater descends by gravity from the 1^{st} to 14^{th} effects achieving a 3 m^3/h nominal distillate production. It was manufactured and delivered by ENTROPIE in 1987. Within the framework of the AQUASOL project in 2005, the original first effect, that worked with low-pressure saturated steam (70 °C, 0.31 bar), was replaced [25]. The new effect allows to work directly with hot water.

The current design specifications are shown in Tab. 1 [14]. The hot water inlet temperature can vary between 57-75 °C exhibiting low deviations in the overall performance ratio [26]. The inlet flow rate can range between 7-12 L/s.

A great amount of seawater is pumped to a condenser placed next to the 14^{th} effect which is used to condense the vapor generated in such effect. The seawater is used for preserving the pressure inside. Part of this seawater is rejected and the remaining part is used to feed the plant. This feed seawater, that can vary between 6-8 m^3/h, is preheated while flows through every effect, and finally in the 1^{st} effect, it is spilt inside the plant. Here, seawater is sprayed over a horizontal-tubes-falling-film-type evaporator whose heat source is hot water coming from the solar field, storage or DEAHP. Part of this seawater evaporates in the effect and the remaining part, more concentrated in salts, falls over the next effect. The vapor produced in the effect flows to the preheater placed next to it where it is partially condensed, releasing this latent heat to the seawater that flows inside the tubes. The distillate and the vapor, which has not condensed, flow to inside the horizontal tube bundle of the next effect. This mixture is used to heat the more concentrated seawater coming from the 1^{st} effect where this process is repeated.

The decreasing pressure arrangement provides an efficient heat transfer between the mixture vapor-distillate and the seawater coming from the previous effect. This is due to the difference between the saturation temperatures of seawater and vapor at same pressure. The pressure drop between effects produces flash evaporation when the seawater enters to the effect. This evaporation decreases the seawater temperature before covering the surface of the tubes. For this reason, seawater has always less temperature than the water which flows inside the tubes.

The vapor condensed by each effect, each preheater and the distillate produced at the final condenser make up the total distillate production of the plant. Part of sensible heat of the distillate is recovered by the plant when flows inside the tube bundle of the effects. In order to improve the process, at PSA-MED

plant the distillate accumulated in one preheater added to the distillate produced in the effect go to the next effect with the exception of cells 4, 7, 13 and 14 as it is shown in Fig. 3.

With the purpose of remove the air and the non-condensable gases generated during the desalination process, two hydro-ejectors are connected to the effects 2, 7 and to the final condenser. This vacuum system removes the gases at the beginning of the experiment, being vapor of water the only gas inside the effects. The hydro-ejectors are within a closed circuit with a tank and an electric pump that drives seawater through the ejectors at a pressure of 3 bar [14].

The supply of seawater is provided by a closed circuit. Two pools are used to store all the seawater: a small pool to mix the distillate and the brine rejected and a bigger one for the supply of the plant. The cooling seawater is spilt into the big pool and part of the heat released by the condenser could increase its temperature during a experiment. To avoid that, a dry cooler is switched on but sometimes it is insufficient [14]. Therefore, it is difficult to obtain a long-steady state in all its variables despite the MED plant has control mechanisms at its inputs.

2.1. Description of the first cell

The first cell of the PSA-MED plant is composed by an effect and a preheater, two horizontal tube bundles, where, over the first one, seawater evaporation is produced and, over the second one, part of the vapor is condensed. Fig. 4 shows a schematic cross section of the first cell.

As commented previously, feed seawater is preheated and pumped to this first cell where a spraying tray sprinkles the seawater over the effect. This spray reaches the first row of the tube bundle and a thin film of seawater is formed over each tube surface. The seawater in the film flows downward due to the gravitational force, falling over all the column tubes. Hot water flows inside the tubes, transferring heat to the thin film. Three water boxes, placed at both sides of the tube bundle, make that the hot water crosses the evaporator four times in a high turbulent flow, decreasing its temperature around 3 °C. Due to the limitations of space and heat power, the actual design of first effect introduces a pressure drop between the inlet and the outlet in nominal conditions of around 0.5 bar.

The vapor produced at the effect flows to the preheater located next to it. A wire mesh demister prevents brine droplets from reaching the preheater tube bundle. When the condensation is produced over the tube surface, a thin film of water is formed. This film slides down due to the gravitational force and it falls over all the column tubes increasing their thickness as more vapor condenses on the film. Seawater flows inside the tubes, acquiring the heat from the condensation. The distillate and part of the vapor generated move to the tubes of the second effect transfering their heats.

The tube bundles are made of 90-10 Cu-Ni with a 14 mm of outside diameter. The heat transfer areas of the effect and the preheater are 24.26 m^2 and 5 m^2, respectively.

3. Thermodynamic properties of seawater

In computational fluid dynamics modeling, the procedure to calculate the thermodynamic properties may be critical. They have a great influence at the error and the computational time of the solutions [27], but also, they are the origin of several problems related with dynamic models, e.g. chattering [28]. Therefore, the computation scheme of thermodynamic properties should meet the requirements of sufficient accuracy, high computing speed, numerical consistency and continuous presentation [29].

Whereas several authors have contributed to the adaptation of thermodynamical properties of water for its use in the computational fluid dynamics modeling area [27, 29, 30, 31, 32] due to its importance

as working fluid in power cycles and numerous other industrial applications, this effort is starting to be done now with other fluids, e.g. seawater [33].

The current procedure to calculate the thermodynamic properties of seawater limits the range of application with respect to dynamic modeling. Sharqawy et al. [34] widely reviewed the main thermodynamic properties of seawater, within of the range of temperature and salinity commonly used in thermal and reverse osmosis seawater desalination applications. Correlations for density, specific heat capacity, thermal conductivity, dynamic viscosity, surface tension, vapor pressure, boiling point elevation, latent heat of vaporization, specific enthalpy, specific entropy and osmotic coefficient were suggested in terms of regression equations as functions of temperature and salinity. Comparisons with other correlations and final recommendations were provided for each property.

The main problem of this set of equations is that they are functions of temperature and salinity, hence these two variables are imposed as state variables. But temperature is not the best state variable in the modeling of two-phase thermal-hydraulics, because it forces to have an additional state variable to fully specify the entire state of the system. To avoid this problem, the most common choice is the specific enthalpy. This variable is not a condition for thermodynamic equilibrium in phase changes, and, it is usually easier to have an explicit dependency of the specific enthalpy at the energy balance equation than other possible variables such as the specific entropy.

One possible solution is to invert the specific enthalpy correlation in order to obtain the temperature as a function of specific enthalpy and salinity. With this inversion it is possible to calculate all other thermodynamic properties in a two-step procedure. Nevertheless, an error produced at the inversion can be spread to all the properties. In the case of Sharqawy et al. [34], the recommended specific enthalpy correlation (Eq. 2) is a third grade polynomial expression, and, therefore it is possible to invert the correlation by an analytical procedure.

Using the specific enthalpy of the water,

$$h_{water} = a_1 + a_2 T + a_3 T^2 + a_4 T^3, \tag{1}$$

the seawater specific enthalpy is calculated as:

$$\begin{aligned} h =& h_{water} - S(b_1 + b_2 + b_3 S^2 + b_4 S^3 + b_5 T + b_6 T^2 \\ &+ b_7 T^3 + b_8 ST + b_9 S^2 T + b_{10} ST^2). \end{aligned} \tag{2}$$

Eq. 1 and Eq. 2 can be reordered obtaining a cubic equation with respect to the temperature:

$$0 = c_4 T^3 + c_3 T^2 + c_2 T + c_1, \tag{3}$$

where,

$$\begin{aligned} c_1 =& a_1 - b_1 S - b_2 S^2 - b_3 S^3 - b_4 S^4 - h, \\ c_2 =& a_2 - b_5 S - b_8 S^2 - b_9 S^3, \\ c_3 =& a_3 - b_6 S - b_{10} S^2, \\ c_4 =& a_4 - b_7 S. \end{aligned}$$

The cubic equation is solvable analytically. Since this coefficients are real numbers, the equation has at least one real solution. Depending on the discriminant it is possible to identify the nature of the other

solutions. Fig. 5 shows an asymptote at $S = 0.01869$, where the equation becomes a quadratic equation. Therefore, the inverse function is divided on three different solutions as a function of the salinity. As Fig. 6 shows, the inverse function is continuous except for small discontinuities at the discriminant asymptote lower than the numerical tolerance of the simulations. The partial derivative with respect to specific enthalpy is also continuous but the partial derivative with respect the salinity presents a discontinuity due to the asymptote. One solution to avoid this discontinuity is to calculate the derivative as the product of other partial derivatives that are continuous applying for that the chain rule.

4. Subsystem Modeling

At §1, it is mentioned that modeling and simulation is a powerful methodology to improve the efficiency of processes. This is because a simulation can predict the plant behavior over different design operating conditions. Due to the complexity of the process, it is important to identify and characterize each one of the subprocesses in order to cover all the dynamics in sufficient grade of detail. For this reason, in this study, the model has been divided into submodels that cover the processes explained in §2.1. The model, as well as the cell, is divided into effect and preheater, two horizontal-tube bundles with different functions: evaporation and condensation. In turn, the tube bundles are divided as function if the process takes place inside or outside the tubes.

4.1. The preheater

4.1.1. Falling film condenser

Condensation happens when the temperature of the vapor is reduced below its saturation temperature. At the horizontal-tube bundle of the preheater, this happens when the vapor comes in contact with the surface of the tubes whose temperature is lower than saturation temperature of the vapor. Even though two different modes of condensation exist, namely film condensation and dropwise condensation, film condensation is the dominant mode and it is the only one considered in the model.

When the condensation appears, over the tube surface a thin film of water grows and slides down under gravitational force. Water falls over all the column of tubes increasing their thickness because more vapor condenses on the films. The film thickness determines the mass and heat flow rates.

Based on a previous model [35], the new developed model determines, by an algebraic procedure, the distillate production using only one control volume (CV). The heat transfer between the tube and the condensate is calculated according to the the Nusselt film condensation theory and the Newton's law of viscosity [36]. An average heat transfer coefficient for the tube bundle is proposed assuming that the film drains smoothly over the tube below [37].

$$\bar{\alpha}_c = 0.729 \left(\frac{\rho_c(\rho_c - \rho_{c,sv}) g k_c^3 L_c^*}{2\mu_c(T_{c,sl} - T_{c,w}) r_c N_{c,row}} \right)^{1/4}. \tag{4}$$

Since the film thickness is small and the liquid film temperature varies between vapor saturation temperature at the vapor-film interface and tube temperature at the tube surface, an usual assumption is to evaluate the thermodynamic properties of each film at only one average temperature. In order to compensate that the condensate is cooled below the saturation temperature, the latent heat of vaporization is replaced by the modified latent heat of vaporization [37] and defined as follows:

$$L_c^* = L_c + 0.68 C_{p,c}(T_{c,sl} + T_{c,w}). \tag{5}$$

Using the Newton's law of cooling, the total condensation rate by the tube bundle is determined from:

$$\dot{m}_{c,cond} = \frac{\dot{Q}_{c,w}}{L_c^*} = \frac{\max(0, N_{c,col} N_{c,row} \bar{\alpha}_c A_{c,w} (T_{c,sl} - T_{c,w}))}{L_c^*}. \tag{6}$$

Therefore, the falling film condenser model is an algebraic model.

4.1.2. Pipe

Bonilla et al. [38] developed a Modelica library of switching moving boundary models for two-phase flow evaporators and condensers inside tubes. Moving boundary models have the advantage of obtaining accurate simulations of two-phase flow pipes without heavy computational efforts.

For modeling the fluid dynamics inside the preheater tube bundle, a sub-cooled pipe model is used. This model uses only one CV with specific enthalpy and pressure as state variables. Furthermore, it allows spread the flow in parallel pipes without increasing the computational effort. Seawater is used as working fluid and the heat transfer coefficient between the the tube and the liquid is calculated by the Gnielinski correlation [39].

4.2. First effect

4.2.1. Falling film evaporator

Boiling and evaporation are similar processes with the same result: a liquid-to-vapor phase change. Both processes occur when the vapor pressure is lower than the saturation pressure. The main difference between them is where this process takes place: boiling occurs at the liquid-solid interface whereas evaporation at the liquid-vapor interface. While at the boiling the entire mass of liquid have to reach saturation conditions, evaporation only occurs when the gaseous phase, that can be a mixture of different substances, is not saturated with the evaporating substance.

Inside the effect, due to the action of the vacuum system, there is only water in gaseous phase. Therefore, boiling and evaporation occur at the same time and they have been considered the same.

At the falling film evaporator, seawater is sprayed over the first row of the tube bundle. Over the surface of these tubes a thin film of water is formed and it falls over the tubes below. Water evaporation produces, besides a reduction of the film thickness, a rise of the salt concentration which in turn produces a change in transfer rates of mass and heat.

The evaporator model presented in this paper is based on the model presented in [40] and afterwards improved in [35]. The model was developed assuming a homogeneous distribution of the film over the tube and an average heat transfer coefficient for the tube bundle. Neglecting the stuckle mass effect allows to develop an algebraic lumped model where the mass and energy balances are:

$$0 = \dot{m}_{e,in} - \dot{m}_{e,out} - \dot{m}_{e,ev}, \tag{7}$$

$$0 = \dot{Q}_{e,w} + \dot{m}_{e,in} h_{e,in} - \dot{m}_{e,out} h_e - \dot{m}_{e,ev} h_{e,sv}. \tag{8}$$

The evaporated mas flow rate is given by:

$$\dot{m}_{e,ev} = \frac{\max(0, \dot{Q}_{e,w} + \dot{m}_{e,in}(h_{e,in} - h_{e,sl}))}{h_{e,sv} - h_{e,sl}}. \tag{9}$$

The max function guarantees the heating of the inlet mass flow rate until reaching saturation condition before evaporation is produced. The outlet mass fraction is calculated as follows.

$$S_e = \frac{\dot{m}_{e,in} S_{e,in}}{\dot{m}_{e,in} + \dot{m}_{e,ev}}. \tag{10}$$

Just as in the condenser model, the heat flow rate is given by the Newton's Law of cooling.

$$\dot{Q}_{e,w} = N_{e,col} N_{e,row} \bar{\alpha}_e A_{e,w} (T_e - T_{e,w}). \tag{11}$$

A Nusselt number correlation allows to calculate the average heat transfer coefficient:

$$Nu_e = \left(\frac{\bar{\alpha}_e}{k_e} \right) \left(\frac{\nu_e^2}{g} \right)^{1/3}. \tag{12}$$

There are many Nusselt number correlations for falling films evaporators in literature, [41]. Sernas [42] and Rogers et al. [43] propose Eq. 13 for horizontal tube bundles with different values for the coefficients. Due to the likely accumulation of dirt in the tubes, these coefficients must be adjusted with real data in order to accurately predict the heat transfer. The results of this calibration are shown in §5.

$$Nu_e = n_1 Re_e^{n_2} Pr_e Ar_e^{n_3}. \tag{13}$$

4.2.2. Pipe

As in §4.1.2, the fluid dynamics inside the effect tube bundle have been modeled using the previously presented library of switching moving boundary models. In this case, the same sub-cooled model has been used. In §2.1, it was explained that the working fluid, hot water, crosses four times the effect. In order to avoid a higher computational effort, a quarter of the total parallel tubes, but with four times their lengths, has been considered.

4.3. Additional models

For assembling the model of the fist cell of the PSA-MED plant, additional models were required.

4.3.1. Wall

The heat exchange between the inner and outer sides of the tube is calculated by the wall model. Due to the thin thickness of the tube, conduction across the tube was neglected. As both models, the falling film condenser/evaporator model and the pipe model, use only one CV, the wall model assumes a single wall temperature that is the mean wall temperature. It is calculated by Eq. 14 and it is a state variable in the model.

$$\dot{Q}_{ff,w} - \dot{Q}_{pp,w} = m_w C_{p,w} \dot{T}_w. \tag{14}$$

4.3.2. Flash

When liquid gets inside a vessel where the pressure is lower than its saturation pressure, part of it suddenly evaporates until both pressures are the same. This latent heat is used to increase the temperature of the liquid. This process can happen inside the cell when a fast change at the inputs can cause an over-heating of seawater.

The flash model has been developed using a single CV without mass or energy storage and where the latent heat from evaporation is used to cool the seawater until the saturation temperature is reached.

The proposed balances of energy and mass are:

$$0 = \dot{m}_{fl,in} - \dot{m}_{fl,out} - \dot{m}_{fl,ev}, \tag{15}$$

$$0 = \dot{m}_{fl,in} h_{fl,in} - \dot{m}_{fl,out} h_{fl,out} - \dot{m}_{fl,ev} h_{fl,sv}. \tag{16}$$

Where the evaporated mass flow rate is calculated as follows:

$$\dot{m}_{fl,ev} = \frac{\max(0, \dot{m}_{in}(h_{fl,in} - h_{fl,sl}))}{h_{fl,sv} - h_{fl,sl}}. \tag{17}$$

The outlet mass fraction is obtained from a expression similar to Eq. 10.

4.3.3. Pressure flow

The efficiency of the multi-effect process lies in the use of the vapor generated by an effect on the following effect. The movement of this vapor flow is caused by the pressure difference between both effects. With the aim of discharging part of the vapor in the gas model, a pressure flow model has been developed.

The mass flow rate between two volumes at different pressure is calculated using the Bernoulli's principle:

$$\dot{m}_p = A_p \sqrt{2\rho_{p,in}(p_{p,in} - p_{p,out})}. \tag{18}$$

Where the vapor flows through an area, A_p, that it is parameter which is calibrated with experimental data. This process is described in §5.

4.3.4. Gas volume

An auxiliary model for the gaseous phase is required in order to connect the effect with the preheater. The model assumes a homogeneous distribution of the vapor inside the connected vessels and it is modeled as a single CV that fills both volumes. The CV allows mass and energy storage ans its mass and energy balances are:

$$\dot{m}_g = \dot{m}_{g,in} - \dot{m}_{g,out}, \tag{19}$$

$$\dot{H}_g = \dot{m}_g h_g + m_g \dot{h}_g = \dot{m}_{g,in} h_{g,in} - \dot{m}_{g,out} h_g. \tag{20}$$

Where the inlet an outlet mass flow are:

$$\dot{m}_{g,in} = \dot{m}_{e,ev} + \dot{m}_{fl,ev}, \tag{21}$$

$$\dot{m}_{g,out} = \dot{m}_{c,cond} + \dot{m}_p. \tag{22}$$

The inlet specific enthalpy is the average value of both inputs:

$$h_{g,in} = \frac{\dot{m}_{e,ev} h_{e,sv} + \dot{m}_{fl,ev} h_{fl,sv}}{\dot{m}_{e,ev} + \dot{m}_{fl,ev}}. \tag{23}$$

Because of the liquid phase volume of both vessels is negligible if it is compared with the gaseous phase volume, a constant volume is assumed. The ideal gas law as equation of state allows to calculate the pressure with this assumption.

$$p_g V_g = m_g K T_g. \tag{24}$$

5. Simulation

This section shows the simulation of the mathematical models previously introduced in §4. The models have been implemented with the non-propietary Modelica language [44]. This language allows to formulate the problems in an acausal way, being very well suited for representing physical systems. Moreover, Modelica is an object-oriented language, therefore, Modelica component diagrams can be encapsulated in classes and hierarchical structures can be created. Dymola 2014 [45] was the Modelica tool used for these simulations. The numerical solver used was DASSL [46] where the relative tolerance was set to 10^{-4}.

Fig. 7 shows the encapsulation of two submodels, the effect and the preheater, and the final model of the first cell. The assembled model (Fig. 7c) has as inputs two fluid sources, one for the feed seawater

(*Sourcef*) and another for the hot water (*Sourceh*), and two additional inputs for the derivatives of the inlet specific enthalpies of both sources. As outputs the model has three sinks that represent the boundaries of the model: *Sinkh* for the effect hot water outlet, *Sinkf* for the effect seawater outlet and *Sinkv* for the preheater vapor and distillate outlet.

The experimental measures, used as inputs in the simulations, are the mass flow rate and the inlet temperature of the hot water, the mass flow rate and inlet temperature of the feed seawater and the pressure of the second effect. The measures used in the calibration and validation are: the outlet temperature of the hot water, the outlet temperature of the feed seawater at the preheater and the pressure of the first effect.

The calibration was accomplished with data from the experiment performed the 14^{th} October 2013. The calibration was carried out by parts (effect, preheater and final model) using the Modelica Optimization library. The obtained calibrated parameter values were $n_1 = 0.2365$, $n_2 = 0.5939$ and $n_3 = -0.1624$ from Eq. 13 and $A_p = 0.0019$ m^2 from Eq. 18.

The validation day selected was the 18^{th} October 2013. In this day, the experimental plant was only operated in the solar mode and the inputs were varied over all the operation range. The measured data were filtered by a low-pass filter with a cutoff frequency of $2 \cdot 10^{-2}$ Hz for reducing the noise in the signals.

In order to avoid initialization problems, the simulation starts with non-zero mass flow rates at both inputs, hot water and feed seawater. Their values changed several times along the experiment as it is shown in Fig. 8a. The inlet hot water temperature also changes several times (Fig. 8b) with the purpose of verifying that the model has a good response in all the operation range. The inlet feed seawater temperature in the preheater is subjected to the heat transfer from the previous preheaters. As it is commented in §2, the seawater is in a closed circuit and, therefore, the inlet feed seawater has a constant salinity of $S = 0.003326$. The second effect pressure is also an uncontrolled variable, its value depends on the heat contribution from the previous and following effects. This is shown in Fig. 9a.

The simulations have been performed starting from steady-state initial conditions, but the system was not in a steady state. For this reason, it can be observed a jump in the evaporated and condensate mass flow rates at the beginning of the simulation in Fig. 9b. These divergences did not affect the rest of the simulation. The CPU-time for integration was 6.54 s in a common laptop (i5 hyper-threaded dual-core processor with 8 Gbytes of RAM), and the simulation presented 4 state events. Outlet hot water and outlet seawater temperatures and first effect pressure, showed good agreement with respect to experimental data in the simulation (cf. Fig. 8b and c and Fig. 9a). Fig. 10 depicts with more detail the error in the simulations. Although the absolute error exceeds the uncertainty range of the measurement instruments in certain ocassions, the average error reveals the goodness of fit obtained with the model since it is lower than the uncertainty range.

Fig. 9b depicts the evolution of the vapor flows in first cell of the MED plant. The simulation shows flash evaporation in a given moment of the experiment. This kind of evaporation process penalizes the heat transfer between hot water and seawater and it is recommendable to avoid it at the first cell. The condensation flow is always much lower than the evaporation flow, so, most of the vapor latent heat is used on the second effect.

As Fig. 9c shows, the outlet salinity of the model varies between $3.35 \cdot 10^{-4}$ and $3.45 \cdot 10^{-4}$ depending on the particular inputs.

6. Conclusions

A new dynamic model of the first cell of a solar-assisted MED plant has been developed. The non-linear model is based on physical principles and predicts the thermal behavior of the plant. It has been developed using the object-oriented Modelica language and it has been calibrated and successfully validated against experimental data from the PSA solar thermal desalination plant. The model includes an empirical heat transfer correlation for the effect and a complete library of thermodynamic properties of seawater. The good agreement between simulation results and experimental data is shown in §5 where the simulation average error is lower than the uncertainty range of the measurement instruments.

The developed model can be used to study the plant performance in different scenarios and operating strategies to optimize future operating control strategies. Its low computational effort allows to use it in fast simulation for testing control algorithms.

The good simulation results encourage us to continue with the development of a dynamic model for the 14-effect distillation plant with the same assumptions considered in this article. Another future goal is to develop a control system to optimize the energy consumption of the plant.

Acknowledgments

The authors would like to thank to CIEMAT research center, Spanish Ministry of Economy and Competitiveness and ERDF funds for financing this work under the National Plan Project, Predictive control techniques for efficient management of renewable energy microgrids. (POWER), DPI2010-21589-C05-02.

References

[1] S. Kalogirou, Seawater desalination using renewable energy sources, Prog Energ Combust 31 (2005) 242–281.

[2] L. García-Rodríguez, Seawater desalination driven by renewable energies: a review, Desalination 143 (2002).

[3] M. T. Ali, H. E. Fath, P. R. Armstrong, A comprehensive techno-economical review of indirect solar desalination, Renew Sust Energ Rev 15 (2011) 4187–4199.

[4] H. M. Qiblawey, F. Banat, Solar thermal desalination technologies, Desalination 220 (2008) 633–644.

[5] H. T. El-Dessouky, H. M. Ettouney, Multiple-effect evaporation desalination systems. thermal analysis, Desalination 125 (1999) 259–276.

[6] H. M. Ettouney, H. T. El-Dessouky, A simulator for thermal desalination processes, Desalination 125 (1999) 277–291.

[7] M. Khademi, M. Rahimpour, A. Jahanmiri, Simulation and optimization of a six-effect evaporator in a desalination process, Chem Eng Process 48 (2009) 339–347.

[8] A. Trostmann, Improved approach to steady state simulation of multi-effect distillation plants, Desalin Water Treat 7 (2009) 93–110.

[9] G. Gautami, S. Khanam, Selection of optimum configuration for multiple effect evaporator system, Desalination 288 (2012) 16–23.

[10] R. Kouhikamali, Thermodynamic analysis of feed water pre-heaters in multiple effect distillation systems, Appl Therm Eng 50 (2013) 1157–1163.

[11] A. M. El-Nashar, Predicting part load performance of small MED evaporators-a simple simulation program and its experimental verification, Desalination 130 (2000) 217–234.

[12] A. M. El-Nashar, Validating the performance simulation program "SOLDES" using data from an operating solar desalination plant, Desalination 130 (2000) 235–253.

[13] P. Palenzuela, D. C. Alarcón-Padilla, J. Blanco-Gálvez, E. Guillén, M. Ibarra, G. Zaragoza, Modeling of the heat transfer of a solar multi-effect distillation plant at the Plataforma Solar de Almería, Desalin Water Treat 31 (2011) 257–268.

[14] P. Palenzuela, D. C. Alarcón-Padilla, G. Zaragoza, J. Blanco-Gálvez, M. Ibarra, Parametric equations for the variables of a steady-state model of a multi-effect desalination plant, Desalin Water Treat 51 (2013) 1229–1241.

[15] A. M. El-Nashar, A. Qamhiyeh, Simulation of the performance of MES evaporators under unsteady state operating conditions, Desalination 79 (1990) 65–83.

[16] N. H. Aly, M. A. Marwan, Dynamic response of multi-effect evaporators, Desalination 114 (1997) 189–196.

[17] D. Kumar, V. Kumar, V. Singh, Modeling and dynamic simulation of mixed feed multi-effect evaporators in paper industry, Appl Math Model 37 (2013) 384–397.

[18] G. Kishore, S. Nisan, S. Dardou, A. K. Adak, V. K. Srivastava, P. K. Tewari, Development of a dynamic simulator (INFMED) for the MED/VC plant, Desalin Water Treat 21 (2010) 364–374.

[19] L. Roca, L. J. Yebra, M. Berenguel, A. de la Calle, Dynamic modeling and simulation of a multi-effect distillation plant, in: Proc. 9th International Modelica Conference, Munich, Germany, 2012, pp. 883–888.

[20] L. Roca, L. J. Yebra, M. Berenguel, D. C. Alarcón-Padilla, Modeling of a Solar Seawater Desalination Plant for Automatic Operation Purposes, J Sol Energy Eng 130 (2008) 041009–1–041009–8.

[21] Y.-D. Kim, K. Thu, A. Myat, K. C. Ng, Numerical simulation of solar-assisted multi-effect distillation (SMED) desalination systems, Desalin Water Treat 51 (2013) 1242–1253.

[22] D. C. Alarcón-Padilla, J. Blanco-Gálvez, L. García-Rodríguez, W. Gernjak, S. Malato, First experimental results of a new hybrid solar/gas multi-effect distillation system: the AQUASOL project, Desalination 220 (2008) 619–625.

[23] E. Zarza, J. Ajona, J. León, A. Gregorzewski, K. Genthner, Solar thermal desalination project at the Plataforma Solar de Almeria, Sol Energ Mater 24 (1991) 608–622.

[24] M. Ibarra, D. C. Alarcón-Padilla, J. Blanco-Gálvez, G. Zaragoza, P. Palenzuela, Performance Of Small Parabolic Through Collector As Thermal Energy Supply To Steam Generation, in: Proc. SolarPACES Conference, Marrakech, Morocco, 2012.

[25] D. C. Alarcón-Padilla, L. García-Rodríguez, Application of absorption heat pumps to multi-effect distillation: a case study of solar desalination, Desalination 212 (2007) 294–302.

[26] P. Fernández-Izquierdo, L. García-Rodríguez, D. C. Alarcón-Padilla, P. Palenzuela, I. Martín-Mateos, Experimental analysis of a multi-effect distillation unit operated out of nominal conditions, Desalination 284 (2012) 233–237.

[27] M. Kunick, H.-J. Kretzschmar, U. Gampe, Fast Calculation of Thermodynamic Properties of Water and Steam in Process Modelling using Spline Interpolation, in: Proc. ICPWS XV, Berlin, Germany, 2008, p. 5.

[28] J. Bonilla, L. J. Yebra, S. Dormido, Chattering in dynamic mathematical two-phase flow models, Appl Math Model 36 (2012) 2067–2081.

[29] X.-D. Wang, B. An, Y.-Y. Duan, Z.-X. Wang, D.-J. Lee, Efficient and accurate computation scheme of p– T thermodynamic properties of water and steam, J Taiwan Inst Chem Eng 43 (2012) 845–851.

[30] X.-D. Wang, Z.-X. Wang, Y.-Y. Duan, B. An, D.-J. Lee, Efficient evaluation of thermodynamic properties of water and steam on p–h surface, J Taiwan Inst Chem Eng (2013).

[31] K. Miyagawa, P. G. Hill, Rapid and Accurate Calculation of Water and Steam Properties Using the Tabular Taylor Series Expansion Method, J Eng Gas Turb Power 123 (2001) 707.

[32] IAPWS, Release on the IAPWS, Industrial Formulation 1997 for the Thermodynamic Properties of Water and Steam, Technical Report, Erlangen, Germany, 1997. URL: http://www.iapws.org/relguide/IF97-Rev.pdf.

[33] IAPWS, Advisory Note No. 5: Industrial Calculation of the Thermodynamic Properties of Seawater, 2013. URL: http://www.iapws.org/relguide/Advise5.pdf.

[34] M. Sharqawy, Thermophysical properties of seawater: A review of existing correlations and data, Desalin Water Treat 16 (2010) 354–380.

[35] A. de la Calle, L. J. Yebra, S. Dormido, Dynamic Modeling and Simulation Study of Falling Film Evaporation and Condensation, in: Proc. 8th EUROSIM Congress on Modelling and Simulation, Cardiff, United Kingdom, 2013.

[36] V. Dhir, J. Lienhard, Laminar Film Condensation on Plane and Axisymmetric Bodies in Nonuniform Gravity, J Heat Trans (1971) 97–100.

[37] F. P. Incropera, T. L. Bergman, D. P. DeWitt, A. S. Lavine, Principles of heat and mass transfer, 7 ed., John Wiley & Sons, 2012.

[38] J. Bonilla, L. J. Yebra, S. Dormido, F. E. Cellier, Object-Oriented Library of Switching Moving Boundary Models for Two-phase Flow Evaporators and Condensers, in: Proc. 9th International Modelica Conference, Munich, Germany, 2012, pp. 71–80.

[39] V. Gnielinski, New equations for heat and mass transfer in turbulent pipe flow and channel flow, Int Chem Eng 2 (1976) 359–368.

[40] A. de la Calle, L. J. Yebra, S. Dormido, Modeling of a falling film evaporator, in: Proc. 9th International Modelica Conference, Munich, Germany, 2012, pp. 941–948.

[41] G. Ribatski, A. M. Jacobi, Falling-film evaporation on horizontal tubes—a critical review, Int J Refrig 28 (2005) 635–653.

[42] V. Sernas, Heat transfer correlation for subcooled water films on horizontal tubes, J Heat Trans 101 (1979) 176–178.

[43] J. Rogers, S. Goindi, M. Lamari, Turbulent falling film flow and heat transfer on horizontal tube, in: Proc. of the National Heat Transfer Conference, Portland, 1995, pp. 3–12.

[44] Modelica Association, Modelica Specification 3.2 Revision 2, 2013. URL: `http://www.modelica.org/documents`.

[45] Dassault Systemes, Dymola 2014 - Dynamic Modeling Laboratory, 2013. URL: `http://www.3ds.com/`.

[46] L. R. Petzold, A description of DASSL: a Diferential/Algebraic System Solver, Scientific Computing (1983) 65–68.

Nomenclature

A	Area (m^2)
Ar	Archimedes number (dimensionless)
a,b,c	Polynomial coefficients (multiple dimensions)
C_p	Specific heat capacity at constant pressure ($J \cdot kg^{-1} \cdot K^{-1}$)
F	Apparent wet area fraction (dimensionless)
g	Gravitational acceleration ($m \cdot s^{-2}$)
H	Enthalpy (J)
h	Specific enthalpy ($J \cdot kg^{-1}$)
L	Latent heat of vaporization ($J \cdot kg^{-1}$)
m	Mass (kg)
N	Number (dimensionless)
Nu	Nusselt number (dimensionless)
n	Nusselt correlation coefficient (dimensionless)
K	Mass gas constant ($J \cdot K^{-1} \cdot kg^{-1}$)
k	Thermal conductivity ($W \cdot m^{-1} \cdot K^{-1}$)
Pr	Prandl number (dimensionless)
p	Pressure (Pa)
Q	Heat (J)
Re	Reynols number (dimensionless)
r	Radius (m)
S	Salinity, salt mass fraction (dimensionless)
T	Temperature (K)
V	Volume (m^3)

Greek symbols

α	Heat transfer coefficient ($W \cdot m^{-2} \cdot K^{-1}$)
μ	Dynamic viscosity ($kg \cdot m^{-1} \cdot s^{-1}$)
ν	Kinematic viscosity ($m^2 \cdot s^{-1}$)
ρ	Density ($kg \cdot m^{-3}$)

Subscripts

c	Falling film condenser
col	Column
cond	Condensate
e	Falling film evaporator
ev	Evaporated
ff	Falling film evaporator or condenser
fl	Flash
fs	Feed seawater
g	Gas volume
hw	Hot water
in	Inlet
mea	Measured
out	Outlet
p	Presure flow
pp	Pipe
row	Row
sim	Simulated
sl	Saturated liquid
sv	Saturated vapor
w	Pipe wall
water	Water

Newton's notation is used for time derivatives.

Table 1: Design specification of PSA-MED plant [14]

Number of effects	14
Heat source energy consumption	200 kW
Performance ratio	>9
Hot water flow rate	12 L/s
Feed seawater flow rate	8 m^3/h
Brine reject	5 m^3/h
Distillate production	3 m^3/h
Top brine temperature	68°C
Condenser temperature	33°C
Vacuum system	Hydroejectors (seawater at 3bar)

Table 2: Seawater specific enthalpy coefficients [34]

i	a_i	b_i
1	$1.41355 \cdot 10^{2}$	$-2.34825 \cdot 10^{4}$
2	$4.20207 \cdot 10^{3}$	$3.15183 \cdot 10^{5}$
3	$-5.35 \cdot 10^{-1}$	$2.80269 \cdot 10^{6}$
4	$4 \cdot 10^{-3}$	$-1.44606 \cdot 10^{7}$
5		$7.82607 \cdot 10^{3}$
6		$-4.41733 \cdot 10^{1}$
7		$2.13940 \cdot 10^{-1}$
8		$-1.99108 \cdot 10^{4}$
9		$2.77846 \cdot 10^{4}$
10		$9.72801 \cdot 10^{1}$

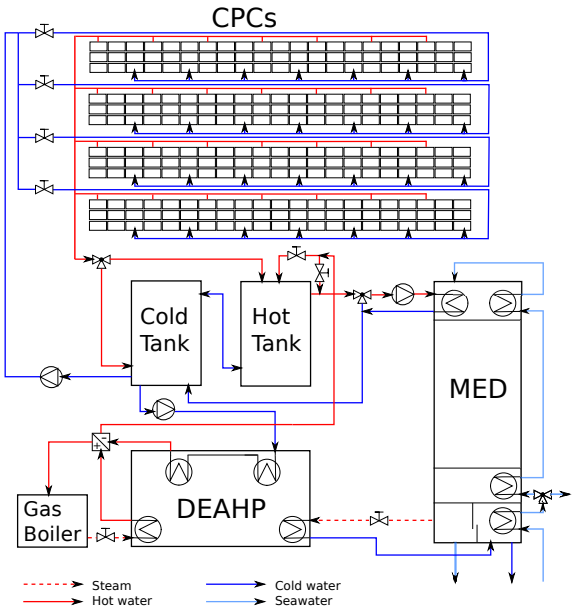

Figure 1: AQUASOL project plant flow sheet

Figure 2: MED plant at PSA

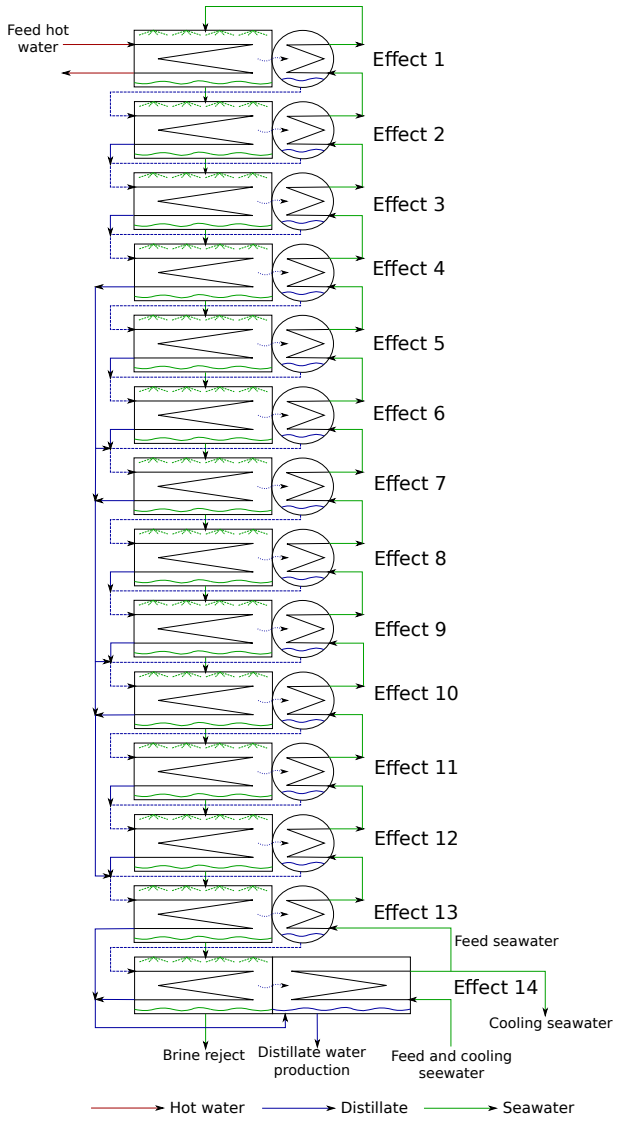

Figure 3: Schematic diagram of the MED plant at PSA

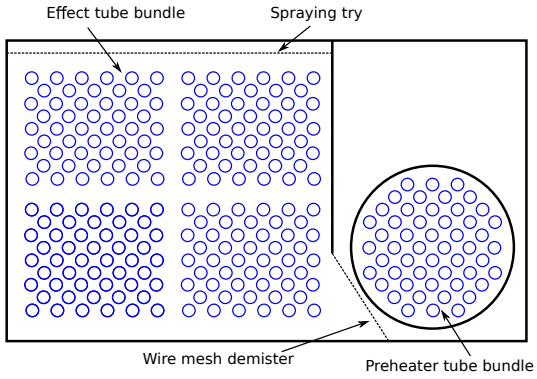

Figure 4: Cross-sectional view of the first cell at PSA

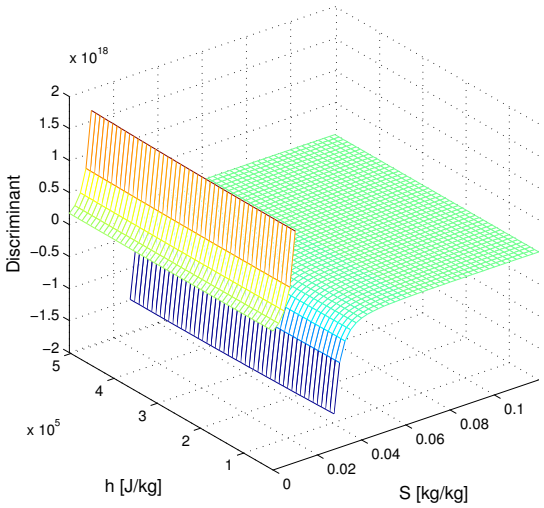

Figure 5: Temperature discriminant as function of specific enthalpy and salinity

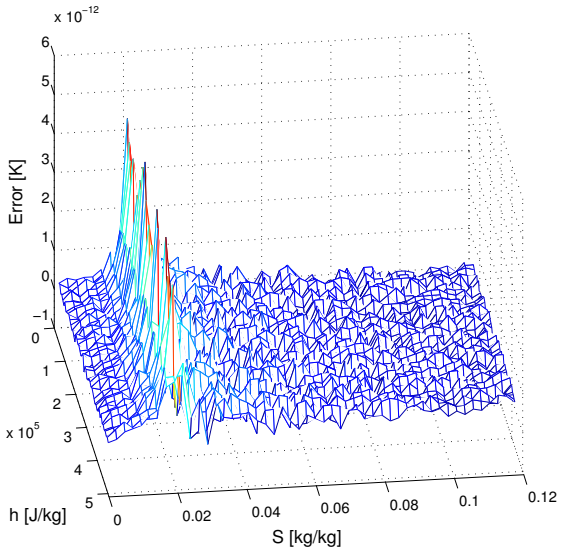

Figure 6: Error of the temperature inverse function

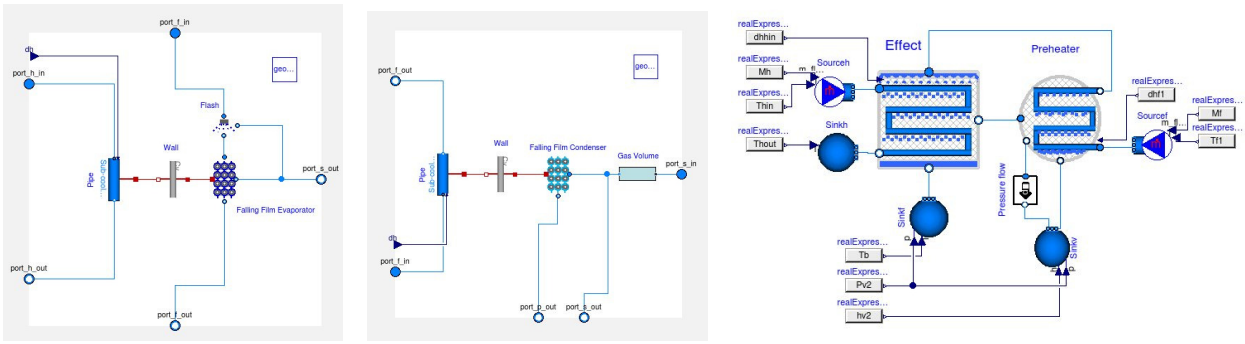

(a) Effect encapsulation (b) Preheater encapsulation (c) First cell final arrangement

Figure 7: Modelica models

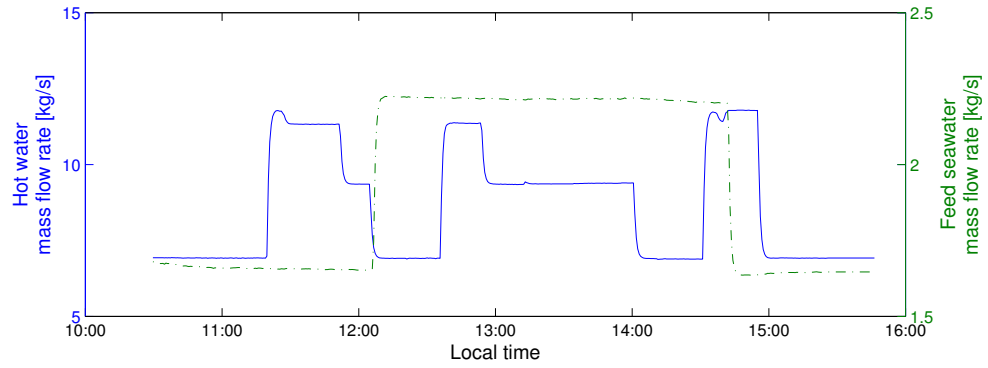

(a) Inlet mass flow rates

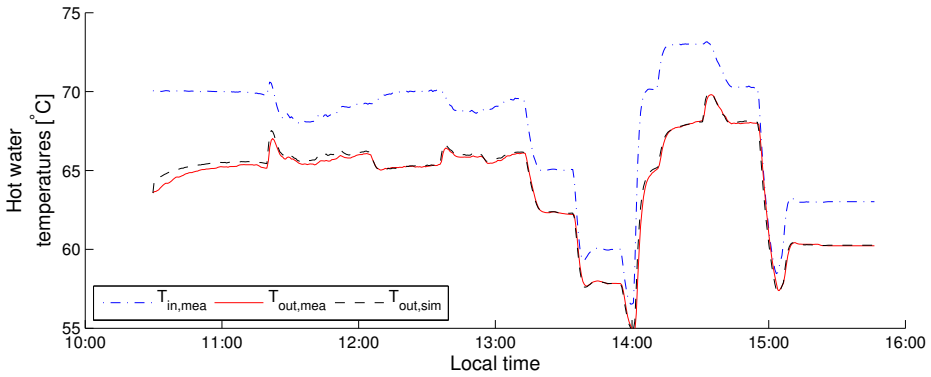

(b) Inlet and outlet hot water temperature

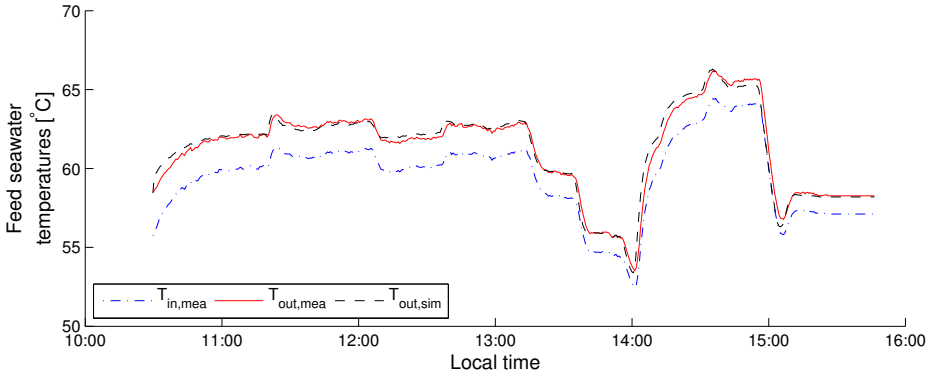

(c) Inlet and outlet feed seawater temperature

Figure 8: Inlets and outlets of the model

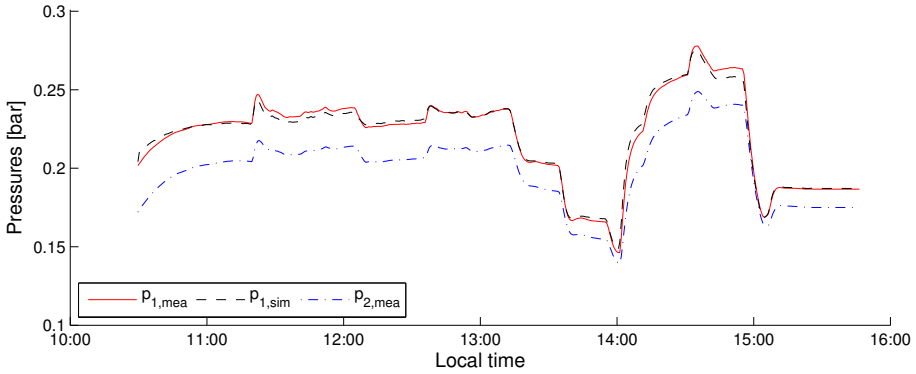

(a) First and second effect pressures

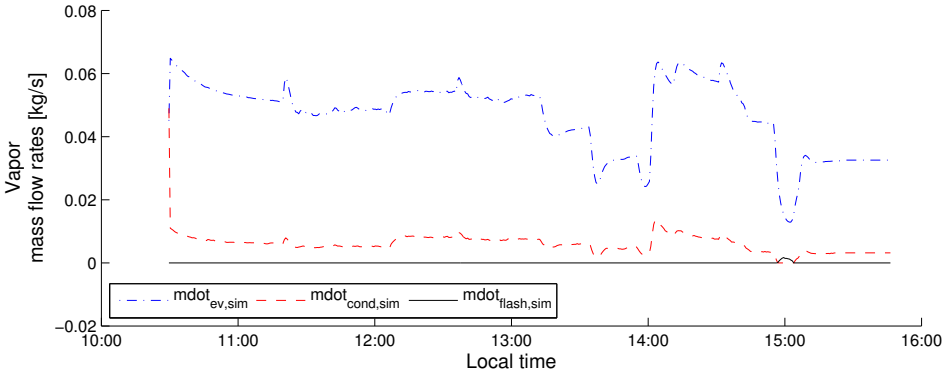

(b) Evaporated and condensation mass flow rates

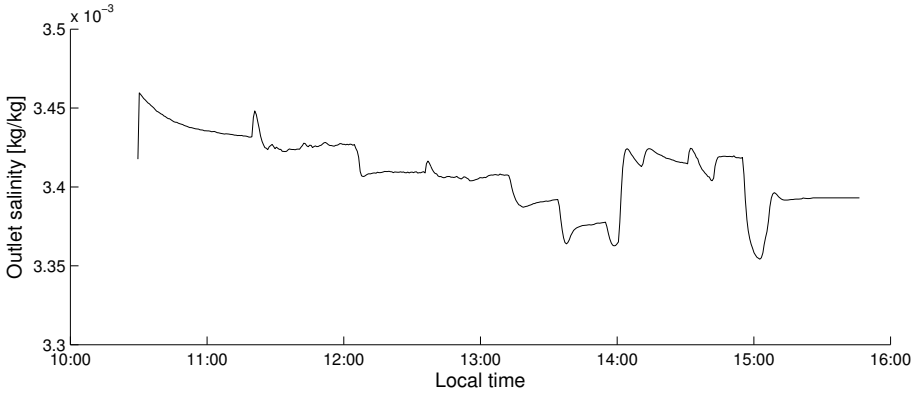

(c) Outlet salinity

Figure 9: Inlets and outlets of the model II

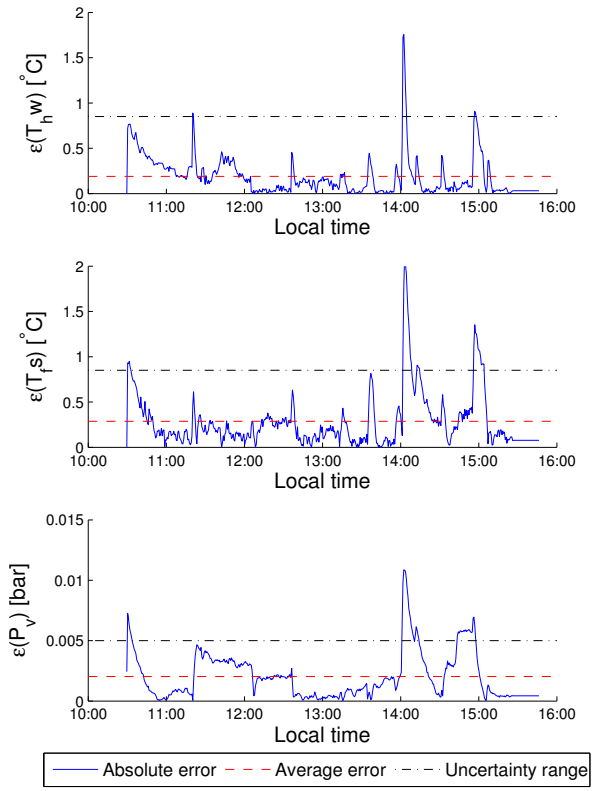

Figure 10: Simulation errors